FRONTIERS OF PHYSICS

RESEARCH ARTICLE
Volume 21 / Issue 12 / 125205 / 2026

Strain-triggered high-temperature superconducting transition in two-dimensional carbon allotrope

Tian Yan[1], Ru Zheng[1], Jin-Hua Sun[1], Fengjie Ma[2], Xun-Wang Yan[3], Miao Gao[1,†], Tian Cui[1,‡], Zhong-Yi Lu[4,§]

1 Department of Physics, School of Physical Science and Technology, Ningbo University, Ningbo 315211, China
2 The Center for Advanced Quantum Studies and Department of Physics, Beijing Normal University, Beijing 100875, China
3 College of Physics and Engineering, Qufu Normal University, Qufu 273165, China
4 Department of Physics, Renmin University of China, Beijing 100872, China
Corresponding authors. E-mail: †gaomiao@nbu.edu.cn, ‡cuitian@nbu.edu.cn, §zlu@ruc.edu.cn
Received January 3, 2026; accepted April 8, 2026

ABSTRACT

Driving non-superconducting materials into a superconducting state through specific modulation is a key focus in the field of superconductivity. Pressure is a powerful method that can switch a three-dimensional (3D) material between non-superconducting and superconducting states. In the two-dimensional (2D) case, strain engineering plays a similar role to pressure. However, purely strain-induced superconductivity in 2D systems remains exceedingly scarce. Using first-principles calculations, we demonstrate that a superconducting transition can be induced solely by applying biaxial tensile strain in a 2D carbon allotrope, THO-graphene, which is composed of triangles, hexagons, and octagons. Free-standing THO-graphene is non-superconducting. Surprisingly, the electron-phonon coupling in strained THO-graphene is enhanced strong enough to pair electrons and realize superconductivity, with the highest superconducting transition temperature reaching 45 K. This work not only provides a notable example of controlling metal-superconductor transition in 2D system just via strain, but also sets a new record of superconducting transition temperature for 2D elemental superconductors. We propose a template-assisted epitaxial growth strategy to obtain THO-graphene, with 2H-$MoTe_2$ as substrate.

Keywords high-temperature superconductivity, two-dimensional carbon allotrope, strain engineering, electron-phonon coupling, first-principles calculation

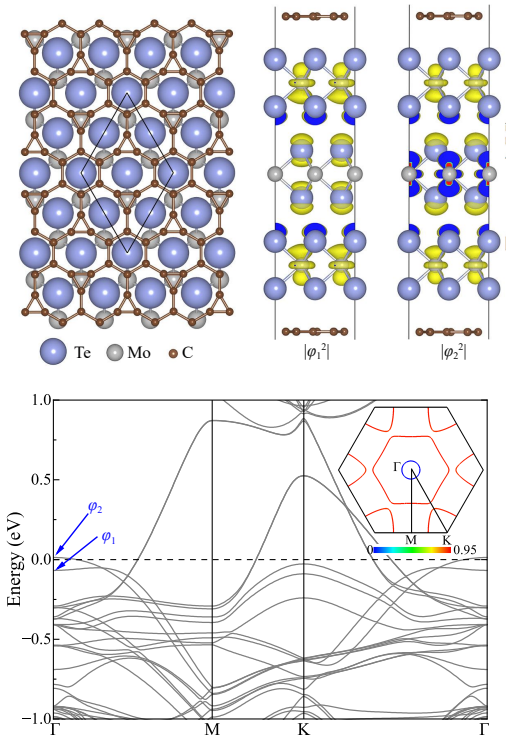

1 Introduction

Applying pressure is regarded as a clean and reversible approach to induce superconductivity in 3D quantum materials without introducing impurities. The compound can always return to its initial non-superconducting state after the removal of pressure. The element crystal of Li becomes superconducting under 48 GPa with

https://doi.org/10.15302/frontphys.2026.125205

superconducting transition temperature (T_c) reaching 20 K [1]. Black phosphorus undergoes a structural transformation from orthorhombic A17 phase to rhombohedral A7 phase at 5 GPa, accompanied by an occurrence of superconductivity [2]. The stripe-type antiferromagnetic order in Mott insulator $BaFe_2S_3$ is destroyed by pressure, with T_c reaching 17 K at 13.5 GPa [3, 4]. The cubic alkali metal fulleride Cs_3C_{60} can be turned into a high-T_c superconductor with pressure close to 1 GPa [5]. The fascinating discovery of novel hydrogen-rich compounds, such as H_3S [6, 7], LaH_{10} [8–11], CeH_{10} [12], CaH_6 [13–15], $(Ca,Y)H_6$ [16–18], $LaBe_2H_8$ [19, 20], LaB_2H_8 [21], and $LaSc_2H_{24}$ [22, 23], provides a pathway to realize room-temperature superconductivity under high-pressure condition. Theoretical calculations play an important role in searching for high-T_c superconductors in the enormous phase space of compressed ternary hydrogen-rich compounds [24–28]. Although kagome metal ATi_3Bi_5 (A = Cs, Rb) are not superconducting at ambient pressure, double-dome superconductivity is observed in both compounds under pressure [29]. Very recently, a pressure of 14 GPa triggers a structural phase transition from ambient-pressure *Amam* phase to a high-pressure *Fmmm* or *I*4/*mmm* phase in bilayer nickelate $La_3Ni_2O_7$, resulting in a superconducting state with T_c achieving 80 K at 18 GPa [30–32].

Acting as a role similar to pressure in the 3D case, strain engineering in 2D system can regulate the in-plane lattice parameters and related electronic properties, providing opportunity for the occurrence or enhancement of superconductivity. FeSe films deposited on $SrTiO_3$ substrate exhibit a dramatic increase of T_c [33], which is closely related to lattice mismatch, charge transfer, and interfacial coupling between electrons of FeSe and high-frequency optical phonons of substrate [34, 35]. Instead of high pressure, $La_3Ni_2O_7$, $La_{2.85}Pr_{0.15}Ni_2O_7$, and $La_2PrNi_2O_7$ thin films facilitated by the application of epitaxial compressive strain show a superconducting transition at ambient pressure [36–38]. Hole doping that introduced by ozone annealing and interfacial diffusion, resulting in the formation of γ pockets at the Fermi surface, is critical to induce superconductivity [39, 40]. For infinite-layer cuprates $Sr_{1-x}Eu_xCuO_{2+y}$, the dome shape of T_c versus doping level of Eu is evidently modulated by tensile strain imposed by $KTaO_3$ substrate [41]. Obviously, purely strain-driven transitions from a non-superconducting to a superconducting state in 2D systems remain extremely rare. Traditional research on 2D superconductivity often relies on doping, substrate effects, or interface engineering. It is quite interesting to find novel 2D materials, in which the superconducting transition can be solely controlled by strain engineering without doping.

Within the framework of electron–phonon coupling (EPC), materials composed of a single light element readily undergo a transition from a non-superconducting to a superconducting state under strain modulation. In terms of electronic structure, single-element systems possess high symmetry and relatively simple band structures, rendering the density of states near the Fermi level extremely sensitive to lattice constant variations. From the perspective of phonons, light-element materials exhibit inherently high phonon frequencies, which can be significantly softened by applied tensile strain. Pristine graphene is a semimetal with vanishing density of states at the Dirac point and exhibits no superconductivity. Theoretical calculation predicted that the T_c of graphene reaches 30 K under hole doping of $\sim 4\times10^{14}$ cm^{-2} and 16.5% BTS [42]. Therefore, to achieve a strain-induced superconducting transition without chemical doping, it is essential to identify 2D metallic materials composed of a single light element.

In this study, we focus on a theoretically proposed 2D carbon allotrope THO-graphene, which was also named as Irida-graphene due to its similarity with the flower Iridaceae [43]. Based on the density functional theory (DFT) first-principles calculations, we find that the EPC of free-standing THO-graphene is too weak to induce superconductivity. After actualizing biaxial tensile strain (BTS), defined by $\epsilon = (a - a_0)/a_0 \times 100\%$ with a_0 and a being the in-plane lattice constants for free-standing and strained case, the strength of EPC is gradually enhanced. THO-graphene undergoes a superconducting transition at BTS about 6%, with T_c being 0.1 K. Further increasing BTS to 12%, the EPC constant λ is substantially elevated to 1.07, owing to softened phonons and enlarged density of states (DOS) at the Fermi level, accompanied by a dramatic elevation of T_c to 45 K. The T_c of THO-graphene predicted in this study sets a new record for 2D elemental superconductor. While the enhancement of the EPC matrix elements has a certain effect on raising the T_c, it is phonon softening that plays the decisive role. Possible routine for the synthesis of THO-graphene is discussed. The electronic structure, lattice dynamics, EPC, and superconductivity of 12%-strained THO-graphene are given in the main text, results for the intermediate BTS and high-order corrections are included in the supplemental material.

2 Calculation methods

In our calculations, the first-principles plane-wave package, QUANTUM-ESPRESSO, is adopted [44]. A vacuum layer of 20 Å is added along the c axis to avoid the coupling between adjacent THO-graphene sheets. We calculate the electronic states by using the generalized gradient approximation (GGA) of Perdew–Burke–Ernzerhof formula [45] and the optimized norm-conserving Vanderbilt pseudopotentials [46]. After full convergence test, the kinetic energy cutoff and the charge density cutoff are set to 80 Ry and 320 Ry, respectively. The

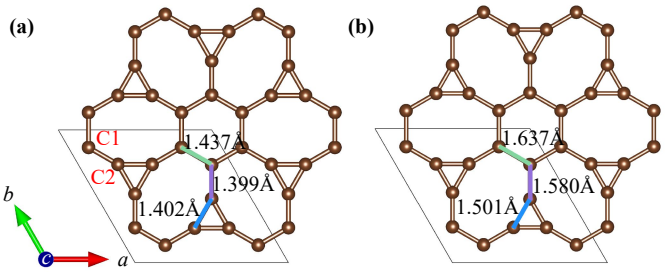

Fig. 1 The crystal structures of THO-graphene. **(a)** Free-standing THO-graphene, in which two inequivalent carbon atoms are labelled as C1 and C2. **(b)** THO-graphene under biaxial tensile strain of 12%. Three distinct C–C bonds are represented by different colors, with bond lengthes marked along the C–C bond. The unit cell is denoted by solid black lines.

charge densities are determined self-consistently on an unshifted mesh of 24×24×1 points with a Methfessel-Paxton smearing [47] of 0.02 Ry. The dynamical matrices and perturbation potentials are calculated on a Γ-centered mesh of 8×8×1 points, within the framework of density-functional perturbation theory [48].

The maximally localized Wannier functions (MLWFs) [49] of strained THO-graphene are constructed on a 8×8×1 grid within the Brillouin zone. We used thirty Wannier functions to describe the band structure of THO-graphene around the Fermi level. More specifically, 12 Wannier functions correspond to the p_z orbitals of carbon atoms, other 18 Wannier functions are σ-like states localized in the middle of carbon-carbon bonds. After minimization, the maximal spatial extension of these MLWFs is smaller than 1.1 Å^2, showing excellent localization. Fine electron (240×240×1, 160×160×1, 80×80×1) and phonon (80×80×1) grids are employed to interpolate the EPC constant with the Wannier90 and EPW codes [50]. Dirac δ-functions for electrons and phonons were replaced by smearing functions with widths of 20 and 0.5 meV, respectively. The convergence test of EPC constant and spatial localities of electronic Hamiltonian and EPC matrix elements are shown in Fig. S1. The superconducting properties of THO-graphene are extensively examined by solving the anisotropic Eliashberg equations [50] using 80×80×1 mesh for both electrons and phonons.

3 Results and discussion

THO-graphene crystallizes in space group $P6/mmm$, where a regular hexagon is surrounded by six octagons, as shown in Fig. 1. For free-standing case, the in-place lattice constant is optimized as 6.315 Å. The two inequivalent carbon atoms locate at Wyckoff positions 6l (0.869, 0.737, 0.000) and 6l (0.741, 0.481, 0.000). Three different types of carbon–carbon bonds serve to link

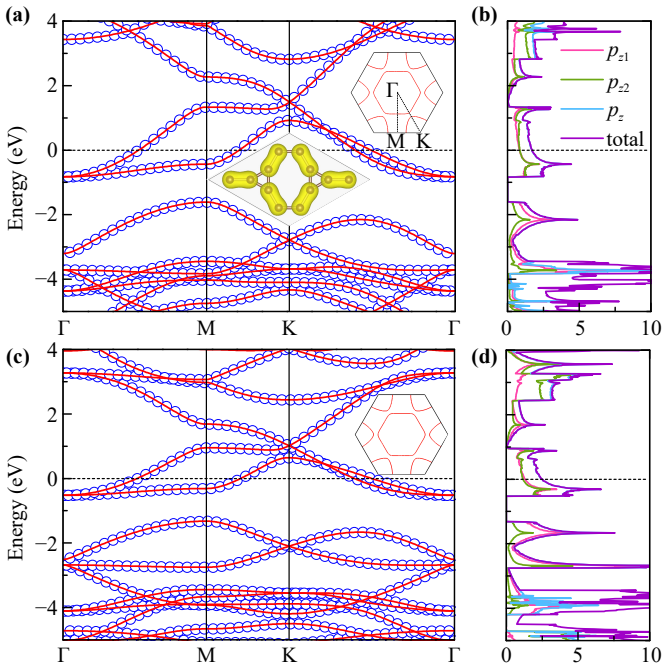

Fig. 2 Electronic structures of THO-graphene. **(a, c)** Band structure of THO-graphene at BTS = 0 and 12%. The red lines and blue circles denote the band structures obtained by the first-principles calculation and the MLWF interpolation, respectively. The Fermi level is set to zero. **(b, d)** Total and p_z-orbital-resolved DOS (states/eV/cell) of THO-graphene at BTS = 0 and 12%. p_{z1} and p_{z2} denote the p_z orbitals of inequivalent carbon atoms marked in Fig. 1.

three specific pairs of polygons: octagon with hexagon, two octagons, and octagon with triangle, respectively. The bond lengths are determined to be 1.402 Å, 1.437 Å, and 1.399 Å, respectively. THO-graphene can withstand a maximum biaxial tensile strain of 12% with the lattice constant being 7.073 Å, before losing its dynamical stability. At this critical BTS, the coordinates of the two inequivalent carbon atoms slight shift to 6l (0.866, 0.733, 0.000) and 6l (0.737, 0.475, 0.000). There types of C–C bonds are elongated to 1.637 Å, 1.580 Å, and 1.501 Å, increasing by 13.92%, 12.94%, and 7.06%, respectively, with respect to the strain-free case.

The electronic structures of free-standing THO-graphene and those under critical BTS of 12% are presented in Fig. 2. THO-graphene is metallic, with two energy bands across the Fermi level [Fig. 2(a)], giving rise to Fermi surfaces that composed of a hexagonal electron Fermi sheet close to the Γ point and a hole Fermi sheet around the K point [see insert in Fig. 2(a)]. Around the Fermi level, the DOS is dominated by p_z orbital of carbon atom [Fig. 2(b)]. This means that states associated with in-plane sp^2-hybridized σ bonds shrink well below the Fermi level and has no contribution to conductivity. To ambiguously determine the bonding nature of THO-graphene in the vicinity of the Fermi level, we further calculate the integrated local DOS from

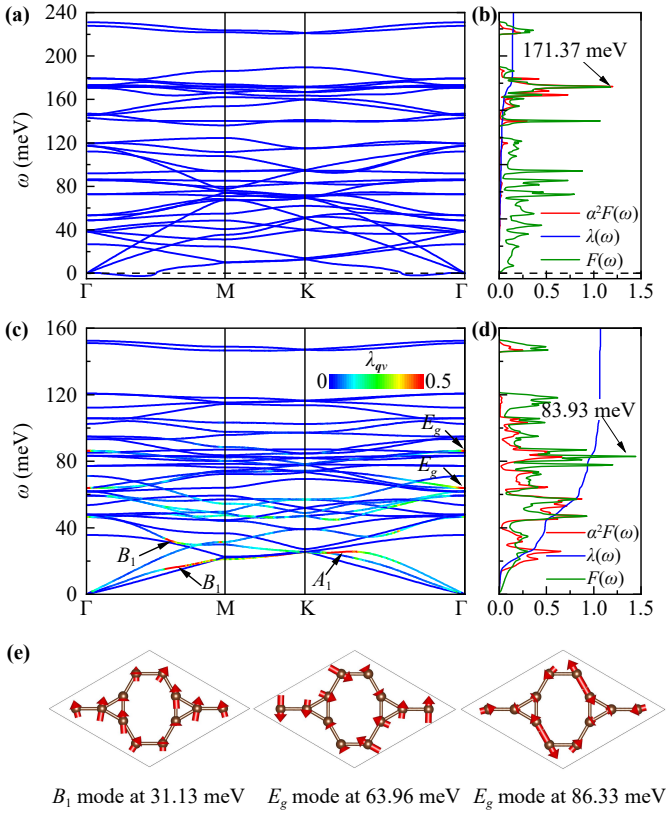

Fig. 3 Lattice dynamics of THO-graphene. **(a, c)** Phonon spectrum of THO-graphene at BTS = 0 and 12%. The strength of $\lambda_{q\nu}$ for each phonon mode $q\nu$ is mapped by different color. **(b, d)** Phonon density of states $F(\omega)$ (modes/meV), Eliashberg spectral function $\alpha^2F(\omega)$, and the resulting $\lambda(\omega)$ after summation at BTS = 0 and 12%. Here, $\lambda(\omega) = 2\int_0^{\omega'} \frac{\alpha^2F(\omega')}{\omega'} d\omega'$. **(e)** The phonon displacements of three optical strongly-coupled phonon modes. The length of red arrow denotes the vibrational amplitude.

–0.1 eV to 0.1 eV. As revealed, the Fermi surface states stem from π-bonding states surrounding the triangles. Consequently, two inequivalent carbon atoms have almost the same weight for the DOS around the Fermi level [Fig. 2(b)]. Under BTS, although the Fermi surfaces are almost unchanged [Fig. 2(c)], the bandwidths are significantly narrowed, leading to an enlarged DOS [Fig. 2(d)]. For example, $N(0)$, DOS at the Fermi level, increases by 45.6% in comparison with the strain-free case, which may be beneficial to superconductivity.

The phonon spectra and DOS $F(\omega)$ for strain-free and 12%-strained THO-graphene are given in Figs. 3(a)–(d). Although several tiny imaginary frequencies near the Γ point are observed in free-standing THO-graphene [Fig. 3(a)], which disappear in the strained case [Fig. 3(c)]. Beside those imaginary modes, other phonon modes have positive frequencies. This phenomenon does not correspond to dynamical instability of the lattice [51], and is commonly found in 2D materials simulations, such as in borophene [52–54], arsenene [55, 56], and honeycomb structures of group-IV elements and III-V binary compounds [57]. We further perform *ab initio* molecular dynamics simulation at 300 K to confirm the stability of this material under realistic conditions. The results evidently demonstrated that the structure remains intact up to 5 ps, with atoms oscillating around their equilibrium positions without any bond breaking or phase transition [Fig. S2], consistent with previous calculation obtained at 1000 K [43]. This provides strong evidence for the dynamical and thermal stability of the material at finite temperatures. The highest phonon frequency of unstrained THO-graphene reaches 231.05 meV, even higher than that of graphene [58, 59]. This is probably related to the short bond length in the carbon triangle. Due to weakening of interatomic force constants induced by BTS, the maximal phonon frequency decreases to 152.44 meV for BTS being 12%, indicating a clear phonon softening. Similarly, the phonon DOS peak shifts from 171.37 meV to 83.93 meV.

To investigate the EPC properties, we calculate the Eliashberg spectral function $\alpha^2F(\omega)$. As revealed by $\alpha^2F(\omega)$ shown in Fig. 3(b), only high-frequency phonons above 130 meV have contribution to the EPC in free-standing THO-graphene. The consistency of $\alpha^2F(\omega)$ and $F(\omega)$ in the high-frequency region indicates that the EPC matrix elements are almost uniformly distributed for these phonons. When the Eliashberg spectral function $\alpha^2F(\omega)$ has substantial weight in the high-frequency region, the resulting EPC constant λ tends to be smaller, since $\lambda = 2\int \frac{\alpha^2F(\omega)}{\omega} d\omega$. As a result, λ equals to 0.15 for unstrained THO-graphene. And no superconductivity can be found by setting the Coulomb pseudopotential μ^* to 0.1. Interestingly, $\alpha^2F(\omega)$ is markedly red-shifted by applying 12% BTS. Several phonon modes make significant contributions to EPC, including the acoustic B_1 and A_1 modes, and two optical E_g modes around 63.96 meV and 86.33 meV [Fig. 3(d)]. The phonon displacements of these strongly-coupled optical modes are depicted in Fig. 3(e), which correspond to the in-plane vibrations of carbon atoms. The EPC constant λ is dramatically enhanced to 1.07, about seven times that of the unstrained case, benefiting from phonon softening. Although, the logarithmic average frequency $\omega_{\log}$ decreases to 39.45 meV, the superconducting T_c is raised to 35.2 K, as roughly estimated by the McMillan-Allen-Dynes formula (T_c^{MAD}) [60, 61]. The key physical parameters of THO-graphene under intermediate BTS are summarized in Table 1. The evolutions of phonons, $F(\omega)$, $\alpha^2F(\omega)$, and $\lambda(\omega)$ under BTS of 8%, 9%, 10% and 11% are given in Fig. S3.

We further solve the anisotropic Eliashberg equations to obtain a reasonable value of T_c and have a insight into the distribution of superconducting gaps for BTS being 12%. Here, the truncated frequency ω_c for the sum over Matsubara frequencies is selected as 1.5 eV, about 10 times that of the highest phonon frequency of THO-

Table 1 Calculated $N(0)$, EPC properties, and T_c under different BTS. $\omega_{\log}$ and $\sqrt{\langle\omega^2\rangle}$ are characteristic phonon frequencies defined in McMillan–Allen–Dynes formula [60, 61]. T_c^{MAD} stands for T_c evaluated by the semi-empirical McMillan–Allen–Dynes formula. T_c^{Aniso} is the T_c value determined by solving the anisotropic Eliashberg equations.

BTS	Doping	$N(0)$	$\omega_{\log}$	$\sqrt{\langle\omega^2\rangle}$	λ	T_c^{MAD}	T_c^{Aniso}
0%	0	1.72	144.39	158.39	0.15	0	–
6%	0	2.07	102.48	111.74	0.26	0.1	–
8%	0	2.20	85.56	94.94	0.35	1.7	–
9%	0	2.28	76.22	85.96	0.42	4.6	–
10%	0	2.35	66.35	76.48	0.51	10.5	18.0
11%	0	2.45	54.75	65.72	0.68	20.8	30.0
12%	0	2.52	39.45	52.02	1.07	35.0	45.0
12%	0.3	2.90	14.70	30.39	3.53	53.2	71.0

graphene under BTS of 12%. Figure 4(a) shows the normalized superconducting gap $\Delta_{n\boldsymbol{k}}$ distribution at different temperatures. The superconducting energy gaps grouped together, suggesting a single-gap nature. The highest temperature with nonvanished $\Delta_{n\boldsymbol{k}}$, i.e., T_c, is calculated to be 45 K. At 10 K, the average superconducting gap $\Delta_{n\boldsymbol{k}}^{\mathrm{ave}}$ for THO-graphene is 7.17 meV. The anisotropy ratio of superconducting gap, $\Delta_{n\boldsymbol{k}}^{\mathrm{aniso}}$, defined by $(\Delta_{n\boldsymbol{k}}^{\mathrm{max}}-\Delta_{n\boldsymbol{k}}^{\mathrm{min}})/\Delta_{n\boldsymbol{k}}^{\mathrm{ave}} = (7.22–7.09)/7.17 = 1.81\%$. The single-gap characteristic is also confirmed by the quasiparticle density of states $N_s(\omega)/N(0)$ [see Fig. 4(c)]. The distribution of superconducting gap $\Delta_{n\boldsymbol{k}}$ on the Fermi surface at 10 K is given in Fig. 4(b), in which the gaps on hexagon-shaped Fermi surface around the Γ point are slightly larger. This is also the case for the distribution of $\lambda_{n\boldsymbol{k}}$ on the Fermi surface [Fig. 4(d)].

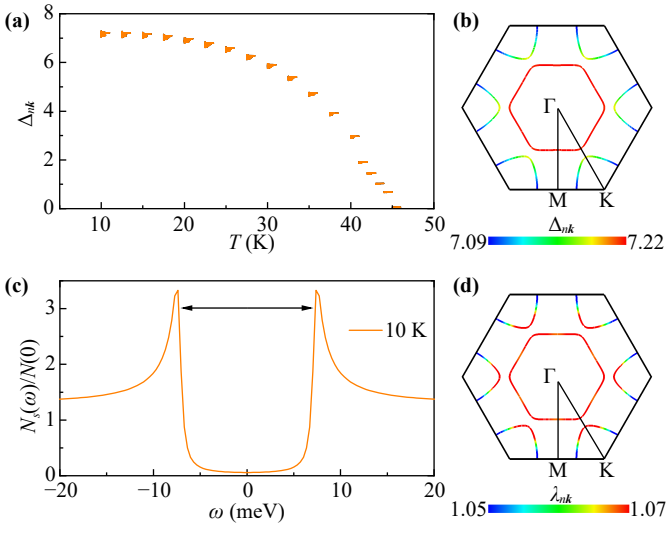

Fig. 4 **(a)** Temperature dependence of the superconducting gap values $\Delta_{n\boldsymbol{k}}$ on the Fermi surface at different temperatures. **(b)** Distribution of superconducting gap $\Delta_{n\boldsymbol{k}}$ on the Fermi surface at 10 K. **(c)** Quasiparticle density of states at 10 K. **(d)** Distribution of EPC strength $\lambda_{n\boldsymbol{k}}$ on the Fermi surface. Here, n and $\boldsymbol{k}$ represent the band index and the momentum of electronic state, respectively.

Intuitively, hole doping can increase $N(0)$, which is beneficial for superconductivity. Our calculations show that at a BTS of 12% and a hole doping concentration of 1.0 hole/cell, a van Hove singularity can be aligned with the Fermi level, leading to a significant increase in $N(0)$ (Fig. S4). However, phonon calculation reveals that under such doping concentration, the system exhibits pronounced dynamical instability, as evidenced by the appearance of extensive imaginary frequencies in the phonon spectrum [Fig. S5(a)]. This is also the case for 0.5 hole/cell doping [Fig. S5(b)]. Through systematic testing, we eventually identified that at a doping concentration of 0.3 hole/cell, the phonon spectrum shows dynamical stability [Fig. S5(c)]. We further perform Wannier interpolation to evaluate EPC strength, which significantly increase to 3.53 (Tabel 1), resulting a T_c as high as 71 K (Fig. S6). Comparing the undoped and doped cases, $N(0)$ increases by only 15.1%, which is insufficient to account for a more than threefold increase in the EPC constant. From another perspective, hole doping can reduce the occupation of bonding states and the bond energy, thereby leading to phonon softening and an increase in EPC strength. Notably, $\omega_{\log}$ softens to one-third of undoped case, the enhancement of EPC and the T_c most likely originate from phonon softening.

To figure out the underlying mechanism for enhanced EPC, we calculate the Fermi surface nesting function $\xi(\boldsymbol{q})$, EPC matrix elements weighted Fermi surface nesting function $\gamma(\boldsymbol{q})$, and wavevector-resolved EPC constant $\lambda(\boldsymbol{q})$, with definitions shown in Fig. 5. Since the superconducting transition occurs at a critical biaxial tensile strain of 6%, we compare above three quantities between 6%- and 12%-strained cases. With respect to that under 6% strain, $N(0)$ increase by 21.7% in 12%-strained case. In general, enlarged $N(0)$ is beneficial to superconductivity. But the rise of $N(0)$ results from bandwidth narrowing induced by BTS, while the shape of the Fermi surface remains unchanged. This leads to small variation in the Fermi surface nesting function $\xi(\boldsymbol{q})$ [Fig. 5(a)]. Therefore, the increase in $N(0)$ does not play a decisive role in enhancing the EPC and the occurrence of superconductivity. After considering the EPC matrix elements on

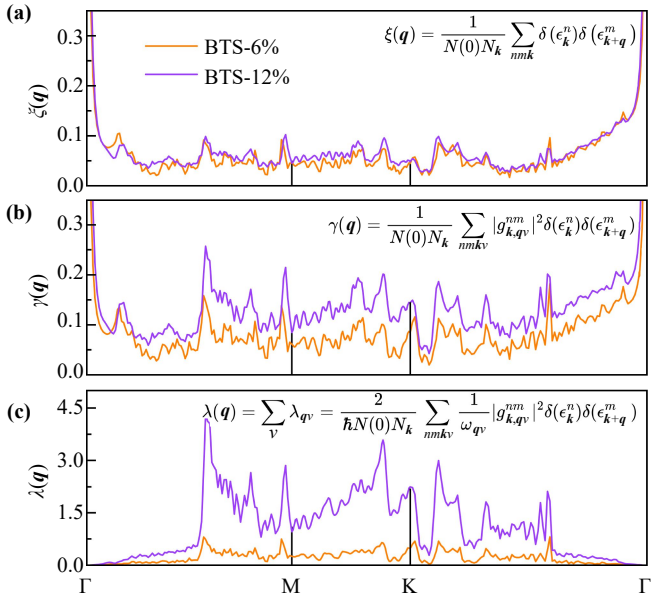

Fig. 5 Fermi surface nesting functions $\xi(\boldsymbol{q})$, EPC matrix elements weighted Fermi surface nesting functions $\gamma(\boldsymbol{q})$, and wavevector-resolved EPC constants $\lambda(\boldsymbol{q})$ in THO-graphene under BTS of 6% and 12%.

the Fermi surface, discrepancy in $\gamma(\boldsymbol{q})$ becomes obvious [Fig. 5(b)], indicating that the enhancement of EPC matrix elements play an important role in the increase of EPC constant λ. Moreover, the difference in $\lambda(\boldsymbol{q})$ exhibits significant amplification, suggesting that enhanced EPC can be mainly attributed to phonon softening [Fig. 5(c)].

We further consider high-level corrections beyond standard GGA, such as van der Waals (vdW) interaction [62], hybrid functional impact [63], and strong correlation effect [64], to verify the robustness of our results. With vdW correction, the lattice constant is optimized to 6.312 Å, exhibiting a slight contraction about 0.003 Å. Moreover, the vdW correction almost has no effect on the band structures of THO-graphene for both unstrained and 12%-strained cases, as shown in Fig. S7. The differences between phonon spectra with and without vdW are indistinguishable, besides the slightly hardened 18th and 36th phonon modes under 12% BTS [Fig. S8]. Specifically, the frequency of the 18th mode at the Γ point increases from 71.16 meV to 72.31 meV after vdW correction. The EPC constant λ, $\omega_{\log}$, and T_c are determined to be 1.01, 41.03 meV, and 43 K for 12%-strained THO-graphene with vdW correction [Table 1 and Fig. S9]. Obviously, these minor variations mentioned above do not significantly affect the EPC and T_c of THO-graphene. The decrease of T_c can be interpreted by phonon hardening. The results obtained with the HSE06 hybrid functional show that THO-graphene remains metallic, and the positions where bands crosses the Fermi level do not change (Fig. S10), indicating that the higher-order hybrid functional correction does not alter the Fermi surface. We approximate the on-site Coulomb interaction within the DFT+U framework (U = 2 and 4 eV). The strong correlation primarily affects the energy bands approximately 3 eV below the Fermi level, leaving electronic states around the Fermi level unchanged [Figs. S11(a) and (b)]. Similarly, phonons only exhibit minor changes after the inclusion of Hubbard U [Fig. S11(c)]. Considering electronic states around the Fermi level and phonons are not changed by HSE06 functional or Hubbard U, we believe that the influence of hybrid functional or strong correlation on superconductivity is small, similar with the case in vdW correction.

Finding high-T_c 2D elemental superconductor is an interesting topic. Beside predicted superconductivity in doped graphene [42], it was reported that twisted bilayer graphene resides in an insulating state, but develops superconductivity with T_c to 1.7 K under electrostatic doping [65]. Since then, the strong correlation and superconductivity in graphene moiré superlattice have drawn lots of attentions [66–68]. T-graphene, a carbon sheet with 4- and 8-membered rings, also named as Octagraphene, was suggested to be an intrinsic elemental superconductor with T_c up to 20.8 K [69]. By disrupting the perfect Fermi surface nesting and long-range magnetic order via electron doping, Octagraphene may exhibit unconventional $s^{\pm}$ superconductivity based on spin fluctuation [70, 71]. Conventional and unconventional superconductivity in biphenylene was investigated, with T_c being 3.0 K and 1.7 K, respectively [72]. Other theoretically studied 2D element superconductor, including silicene [73], phosphorene [74], borophene [52–54], and arsenene [55, 56], were predicted with T_c no more than 31 K. In experiment, growing thin film structure through 3D superconducting noble metal is another strategy to obtain 2D elemental superconductor, for example, Nb [75], Pb [76, 77], Ga [78], and Sn [79] thin films. Therefore, the T_c of THO-graphene set a new record for 2D element superconductor.

For theoretical predictions, strain-induced superconducting transition from a non-superconducting phase is rarely reported. Strain modulation plays a role to enhance the T_c of 2D intrinsic superconductors that proposed theoretically. The transition temperature of monolayer MgB_2 is boosted from 20 K to 50 K under 4% tensile strain [80]. After hydrogenation, the T_c of monolayer MgB_2 is further raised to 67 K due to the reduction of electron occupation in boron σ-bands, and up to 100 K with strain tuning [81]. Sandwich-like trilayer films, formed by two hexagonal BC sheets and a intercalation metal layer in between, e.g., LiB_2C_2 and NaB_2C_2, are promising 2D high-T_c superconductors with the highest T_c achieving 150 K under BTS [82–85]. Strain heightens the EPC of hole-doped hexagonal monolayer BN, leading a maximal T_c of 41.6 K at 17.5%

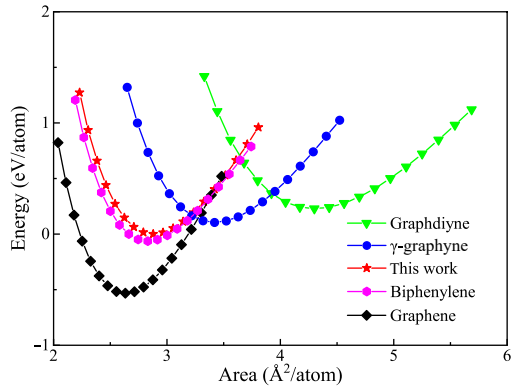

Fig. 6 Total energy comparison among five different 2D carbon allotropes, as a function of area per atom. Here, the total energy of optimized THO-graphene is set to zero.

strain [86]. Three-gap superconductivity was suggested in hydrogenated LiBC with T_c above 120 K under 3.59% tensile strain [87]. Hydrogenated Janus 2H-MoSH displays an intrinsic T_c of 26.8 K, tunable to 36.7 K via strain and doping [88]. Thus, THO-graphene can be regarded as an outstanding platform in which metal-superconductor transition is effectively controlled by applying strain.

To figure out whether it's possible to obtain THO-graphene experimentally, we compare its total energy with respect to four 2D carbon sheets that have been synthesized (Fig. 6), i.e., graphene [89], graphdiyne [90, 91], γ-graphyne [92, 93], and biphenylene [94]. Although THO-graphene is less stable in comparison with graphene and biphenylene, it possesses a lower formation energy than γ-graphyne and graphdiyne, with energy advantages being 105.5 meV/atom and 228.3 meV/atom, respectively. This strongly suggests that there is a probability to acquire THO-graphene in experiment.

Considering the hexagonal symmetry and the lattice constant, we propose a template-assisted epitaxial growth strategy. Particularly, the synthesis of THO-graphene on the MoS_2 and $MoTe_2$ substrates is highly reasonable. This idea is supported by the following two key factors. (i) Exceptional lattice matching. The free-standing THO-graphene exhibits a lattice constant of 6.315 Å. High-T_c state is achieved under a 12% tensile strain with lattice constant being 7.073 Å. These two values align perfectly with the 2×2 supercell lattice constants of 2H-phase MoS_2 and $MoTe_2$, whereas the optimized lattice constants are 3.191 Å for MoS_2 and 3.531 Å for $MoTe_2$. Consequently, their 2×2 supercells measure 6.382 Å and 7.062 Å, respectively, showing excellent coincidence with the unstrained and 12%-strained THO-graphene. This perfect lattice matching is crucial for reducing interfacial defects and strain energy, promoting high-quality epitaxial growth. (ii) Electronic inertness of the substrates. The 2H phases of MoS_2 and $MoTe_2$ are semiconducting [95–97]. The energy

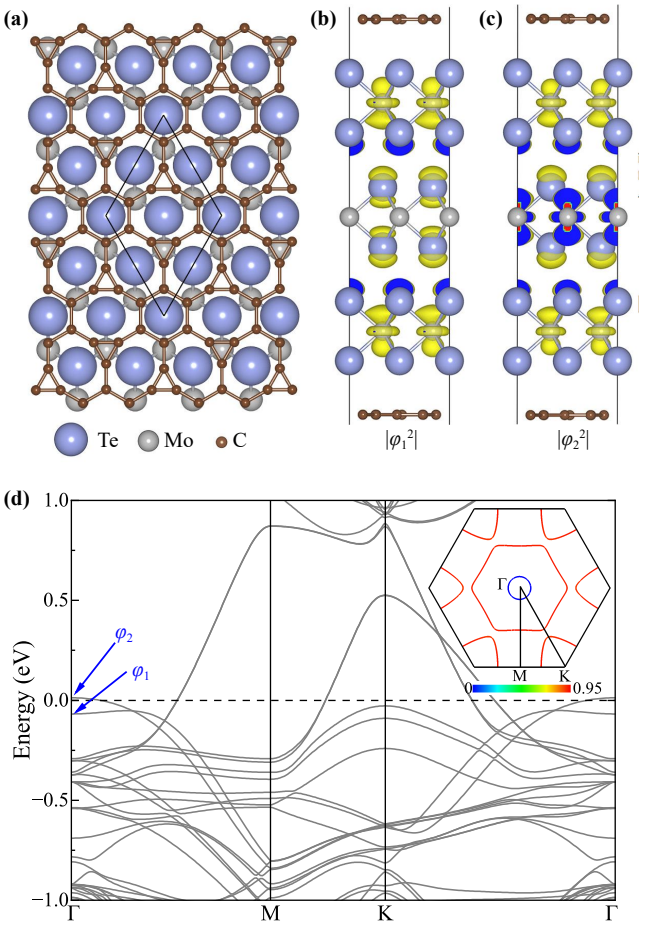

Fig. 7 **(a)** Top view of THO-graphene on 2H-$MoTe_2$ substrate. **(b–c)** Side views of the slab model, with distributions of charge densities for electronic states marked in (d). **(d)** Band structure. The Fermi level is set to zero. States at the Γ point near the Fermi level is denoted as φ_1 and φ_2. The insert shows Fermi surface, with color scale representing the weight of carbon orbitals.

bandgaps ensure that the substrates are electronically inert, showing little hybridization with states of THO-graphene around the Fermi level. This electronic isolation preserves the intrinsic low-energy electronic structure of THO-graphene, allowing its superconducting properties to be examined without interference from the substrate.

We carry out a simulation with THO-graphene on $MoTe_2$ substrate to verify above assumption. A slab model containing $MoTe_2$ trilayer in the middle is adopted, whereas two THO-graphene sheets are included on both sides with mirror symmetry [Figs. 7(a)–(c)]. By fixing the in-plane lattice constant to the bulk value of $MoTe_2$, the deposition of THO-graphene will gain 62.7 meV/carbon atom, suggesting that the synthesis of THO-graphene on $MoTe_2$ substrate is energetically favorable. As revealed by the band structure and Fermi surface, hole pocket around the Γ point is observed [Fig. 7(d) and its insert]. Electronic states at Γ point

near the Fermi level stem from the $MoTe_2$ substrate as shown by the charge density distributions [Figs. 7(b) and (c)]. Beside this hole pocket, other pieces of Fermi surface almost resemble those of free-standing THO-graphene (Fig. 2). Thus, $MoTe_2$ not only provides an ideal substrate with target strained lattice constant, but also has little impact on the electronic structure of THO-graphene in the vicinity of the Fermi level. Consequently, the high-T_c superconductivity can survive. Moreover, the hole pockets associated with $MoTe_2$ may provide additional channels to pair electrons and boost the superconducting T_c.

4 Conclusion

In summary, this study demonstrates the remarkable potential of strain engineering as a powerful and clean tool to induce superconductivity in two-dimensional elemental materials. Through systematic first-principles calculations, we have shown that THO-graphene, a metallic carbon monolayer composed of triangles, hexagons, and octagons, undergoes a dramatic transition from a non-superconducting state to a robust superconductor under applied biaxial tensile strain. The emergence of superconductivity is primarily driven by the synergistic effects of enhanced EPC matrix elements and softened phonons, whereas phonon softening plays a decisive role. These changes collectively enhance the electron-phonon coupling strength, enabling Cooper pair formation. Notably, at a strain of 12%, the calculated T_c reaches 45 K, which represents the highest predicted temperature among purely elemental 2D superconductors reported to date. Further incorporating hole doping, the T_c can be elevated to 71 K. This finding sets a new benchmark and highlights the unique responsiveness of carbon-based nanostructures to mechanical deformation. Furthermore, the energetic feasibility of THO-graphene relative to other synthesized carbon allotropes suggests promising prospects for its experimental realization. Moreover, a template-assisted epitaxial growth strategy with 2H-$MoTe_2$ being the substrate is proposed to synthesize THO-graphene.

Declarations The authors declare that they have no competing interests and there are no conflicts.

Electronic supplementary materials The online version contains supplementary material available at https://doi.org/10.15302/frontphys.2026.125205.

Acknowledgements This work was supported by the National Key R&D Program of China (Grants No. 2024YFA1408601 and No. 2023YFA1406201), Zhejiang Provincial Natural Science Foundation of China (Grants No. LMS26A040005 and No. LMS26A040006), the National Natural Science Foundation of China (Grants No. 12434009 and No. 12274255), the Program for Science and Technology Innovation Team in Zhejiang (Grant No. 2021R01004), and Ningbo Young Scientific and Technological Innovation Leaders Program (Grant No. 2023QL016). F.M. was also supported by the BNU Tang Scholar.

References

1. K. Shimizu, H. Ishikawa, D. Takao, T. Yagi, and K. Amaya, Superconductivity in compressed lithium at 20 K, *Nature* 419(6907), 597 (2002)
2. X. A. Li, J. Sun, P. Shahi, M. Gao, A. H. MacDonald, Y. Uwatoko, T. Xiang, J. B. Goodenough, J. Cheng, and J. Zhou, Pressure-induced phase transitions and superconductivity in a black phosphorus single crystal, *Proc. Natl. Acad. Sci. USA* 115(40), 9935 (2018)
3. H. Takahashi, A. Sugimoto, Y. Nambu, T. Yamauchi, Y. Hirata, T. Kawakami, M. Avdeev, K. Matsubayashi, F. Du, C. Kawashima, H. Soeda, S. Nakano, Y. Uwatoko, Y. Ueda, T. J. Sato, and K. Ohgushi, Pressure-induced superconductivity in the iron-based ladder material $BaFe_2S_3$, *Nat. Mater.* 14(10), 1008 (2015)
4. Y. Oubaid, V. Balédent, O. Fabelo, L. Bocher, C. V. Colin, S. Chattopadhyay, E. Elkaim, M. Verseils, A. Forget, D. Colson, D. Bounoua, P. Fertey, and P. Foury-Leylekian, New insight on the properties of the superconducting iron spin ladder $BaFe_2S_3$, *Front. Phys. (Beijing)* 21(5), 055201 (2026)
5. Y. Takabayashi, A. Y. Ganin, P. Jeglič, D. Arčon, T. Takano, Y. Iwasa, Y. Ohishi, M. Takata, N. Takeshita, K. Prassides, and M. J. Rosseinsky, The disorder-free non-BCS superconductor Cs_3C_{60} emerges from an antiferromagnetic insulator parent state, *Science* 323(5921), 1585 (2009)
6. D. F. Duan, Y. X. Liu, F. B. Tian, D. Li, X. L. Huang, Z. L. Zhao, H. Y. Yu, B. Liu, W. J. Tian, and T. Cui, Pressure-induced metallization of dense $(H_2S)_2H_2$ with high-T_c superconductivity, *Sci. Rep.* 4(1), 6968 (2014)
7. A. P. Drozdov, M. I. Eremets, I. A. Troyan, V. Ksenofontov, and S. I. Shylin, Conventional superconductivity at 203 K at high pressures in the sulfur hydride system, *Nature* 525(7567), 73 (2015)
8. H. Liu, I. I. Naumov, R. Hoffmann, N. W. Ashcroft, and R. J. Hemley, Potential high-T_c superconducting lanthanum and yttrium hydrides at high pressure, *Proc. Natl. Acad. Sci. USA* 114(27), 6990 (2017)
9. F. Peng, Y. Sun, C. J. Pickard, R. J. Needs, Q. Wu, and Y. M. Ma, Hydrogen clathrate structures in rare earth hydrides at high pressures: Possible route to room-temperature superconductivity, *Phys. Rev. Lett.* 119(10), 107001 (2017)
10. A. P. Drozdov, P. P. Kong, V. S. Minkov, S. P. Besedin, M. A. Kuzovnikov, S. Mozaffari, L. Balicas, F. F. Balakirev, D. E. Graf, V. B. Prakapenka, E. Greenberg, D. A. Knyazev, M. Tkacz, and M. I. Eremets, Superconductivity at 250 K in lanthanum hydride under high pressures, *Nature* 569(7757), 528 (2019)
11. F. Hong, L. X. Yang, P. F. Shan, P. T. Yang, Z. Y. Liu, J. P. Sun, Y. Y. Yin, X. H. Yu, J. G. Cheng, and Z. X. Zhao, Superconductivity of lanthanum superhydride investigated using the standard four-probe configuration

under high pressures, *Chin. Phys. Lett.* 37(10), 107401 (2020)
12. W. H. Chen, D. V. Semenok, X. L. Huang, H. Y. Shu, X. Li, D. F. Duan, T. Cui, and A. R. Oganov, High-temperature superconducting phases in cerium superhydride with a T_c up to 115 K below a pressure of 1 megabar, *Phys. Rev. Lett.* 127(11), 117001 (2021)
13. H. Wang, J. S. Tse, K. Tanaka, T. Iitaka, and Y. Ma, Superconductive sodalite-like clathrate calcium hydride at high pressures, *Proc. Natl. Acad. Sci. USA* 109(17), 6463 (2012)
14. L. Ma, K. Wang, Y. Xie, X. Yang, Y. Y. Wang, M. Zhou, H. Liu, X. H. Yu, Y. S. Zhao, H. B. Wang, G. T. Liu, and Y. Ma, High-temperature superconducting phase in clathrate calcium hydride CaH_6 up to 215 K at a pressure of 172 GPa, *Phys. Rev. Lett.* 128(16), 167001 (2022)
15. Z. W. Li, X. He, C. L. Zhang, X. C. Wang, S. J. Zhang, Y. T. Jia, S. M. Feng, K. Lu, J. F. Zhao, J. Zhang, B. S. Min, Y. W. Long, R. C. Yu, L. H. Wang, M. Y. Ye, Z. S. Zhang, V. Prakapenka, S. Chariton, P. A. Ginsberg, J. Bass, S. H. Yuan, H. Z. Liu, and C. Q. Jin, Superconductivity above 200 K discovered in superhydrides of calcium, *Nat. Commun.* 13(1), 2863 (2022)
16. X. W. Liang, A. Bergara, L. Y. Wang, B. Wen, Z. S. Zhao, X. F. Zhou, J. L. He, G. Y. Gao, and Y. J. Tian, Potential high-T_c superconductivity in $CaYH_{12}$ under pressure, *Phys. Rev. B* 99(10), 100505 (2019)
17. H. Xie, D. F. Duan, Z. J. Shao, H. Song, Y. C. Wang, X. H. Xiao, D. Li, F. B. Tian, B. B. Liu, and T. Cui, High-temperature superconductivity in ternary clathrate $YCaH_{12}$ under high pressures, *J. Phys.: Condens. Matter* 31(24), 245404 (2019)
18. K. X. Zhang, J. N. Guo, Y. L. Wang, X. Y. Wu, X. L. Huang, and T. Cui, Robust superconducting stability of ternary hydride $Im\bar{3}m$ (Y, Ca)H_6 upon decompression, *Chin. Phys. Lett.* 42(11), 110704 (2025)
19. Z. H. Zhang, T. Cui, M. J. Hutcheon, A. M. Shipley, H. Song, M. Y. Du, V. Z. Kresin, D. F. Duan, C. J. Pickard, and Y. S. Yao, Design principles for high-temperature superconductors with a hydrogen-based alloy backbone at moderate pressure, *Phys. Rev. Lett.* 128(4), 047001 (2022)
20. Y. G. Song, J. K. Bi, Y. Nakamoto, K. Shimizu, H. Y. Liu, B. Zou, G. T. Liu, H. B. Wang, and Y. M. Ma, Stoichiometric ternary superhydride $LaBeH_8$ as a new template for high-temperature superconductivity at 110 K under 80 GPa, *Phys. Rev. Lett.* 130(26), 266001 (2023)
21. X. X. Song, X. K. Hao, X. D. Wei, X. L. He, H. Y. Liu, L. Ma, G. T. Liu, H. B. Wang, J. Y. Niu, S. J. Wang, Y. P. Qi, Z. Y. Liu, W. T. Hu, B. Xu, L. Wang, G. Y. Gao, and Y. J. Tian, Superconductivity above 105 K in nonclathrate ternary lanthanum borohydride below megabar pressure, *J. Am. Chem. Soc.* 146(20), 13797 (2024)
22. X. L. He, W. B. Zhao, Y. Xie, A. Hermann, R. J. Hemley, H. Y. Liu, and Y. M. Ma, Predicted hot superconductivity in $LaSc_2H_{24}$ under pressure, *Proc. Natl. Acad. Sci. USA* 121(26), e2401840121 (2024)
23. Y. G. Song, C. H. Ma, H. B. Wang, M. Zhou, Y. P. Qi, W. Z. Cao, S. R. Li, H. Y. Liu, G. T. Liu, and Y. M. Ma, Room-temperature superconductivity at 298 K in ternary La–Sc–H system at high-pressure conditions, arXiv: 2510.01273 (2025)
24. M. Gao, X. W. Yan, Z. Y. Lu, and T. Xiang, Phonon mediated high-temperature superconductivity in the ternary borohydride KB_2H_8 under pressure near 12 GPa, *Phys. Rev. B* 104(10), L100504 (2021)
25. M. Gao, P. J. Guo, H. C. Yang, X. W. Yan, F. Ma, Z. Y. Lu, T. Xiang, and H. Q. Lin, Stabilizing a hydrogen-rich superconductor at 1 GPa by charge transfer modulated virtual high-pressure effect, *Phys. Rev. B* 107(18), L180501 (2023)
26. K. Dolui, L. J. Conway, C. Heil, T. A. Strobel, R. P. Prasankumar, and C. J. Pickard, Feasible route to high-temperature ambient-pressure hydride superconductivity, *Phys. Rev. Lett.* 132(16), 166001 (2024)
27. Z. F. Ouyang, B. W. Yao, X. Q. Han, P. J. Guo, Z. F. Gao, and Z. Y. Lu, High-temperature superconductivity in Li_2AuH_6 mediated by strong electron–phonon coupling under ambient pressure, *Phys. Rev. B* 111(14), L140501 (2025)
28. Y. L. Hai, H. J. Yan, and Y. Q. Cai, Structural screening of phosphorus sulfur ternary hydride PSH_6 with a high-temperature superconductivity at 130 GPa, *Front. Phys. (Beijing)* 18(2), 23303 (2023)
29. J. Y. Nie, X. F. Yang, K. Y. Chen, X. Q. Liu, W. Xia, J. Wang, R. Zhang, D. Z. Dai, C. C. Zhao, C. P. Tu, H. L. Dong, X. B. Jin, J. K. Deng, X. Zhang, Y. F. Guo, and S. Y. Li, Pressure-induced double-dome superconductivity in kagome metals ATi_3Bi_5 (A = Cs, Rb), *Chin. Phys. Lett.* 42(7), 070713 (2025)
30. H. L. Sun, M. W. Huo, X. W. Hu, J. Y. Li, Z. J. Liu, Y. F. Han, L. Y. Tang, Z. Q. Mao, P. T. Yang, B. S. Wang, J. G. Cheng, D. X. Yao, G. M. Zhang, and M. Wang, Signatures of superconductivity near 80 K in a nickelate under high pressure, *Nature* 621(7979), 493 (2023)
31. J. Hou, P. T. Yang, Z. Y. Liu, J. Y. Li, P. F. Shan, L. Ma, G. Wang, N. N. Wang, H. Z. Guo, J. P. Sun, Y. Uwatoko, M. Wang, G. M. Zhang, B. S. Wang, and J. G. Cheng, Emergence of high-temperature superconducting phase in pressurized $La_3Ni_2O_7$ crystals, *Chin. Phys. Lett.* 40(11), 117302 (2023)
32. Y. N. Zhang, D. J. Su, Y. E. Huang, Z. Y. Shan, H. L. Sun, M. W. Huo, K. X. Ye, J. W. Zhang, Z. H. Yang, Y. K. Xu, Y. Su, R. Li, M. Smidman, M. Wang, L. Jiao, and H. Q. Yuan, High temperature superconductivity with zero resistance and strange metal behaviour in $La_3Ni_2O_{7-\delta}$, *Nat. Phys.* 20(8), 1269 (2024)
33. Q. Y. Wang, Z. Li, W. H. Zhang, Z. C. Zhang, J. S. Zhang, W. Li, H. Ding, Y. B. Ou, P. Deng, K. Chang, J. Wen, C. L. Song, K. He, J. F. Jia, S. H. Ji, Y. Y. Wang, L. L. Wang, X. Chen, X. C. Ma, and Q. K. Xue, Interface-induced high-temperature superconductivity in single unit-cell FeSe films on $SrTiO_3$, *Chin. Phys. Lett.* 29(3), 037402 (2012)
34. K. Liu, Z. Y. Lu, and T. Xiang, Atomic and electronic structures of FeSe monolayer and bilayer thin films on $SrTiO_3$(001): First-principles study, *Phys. Rev. B* 85(23), 235123 (2012)

35. M. D. Zhang, R. C. Shi, R. Wu, X. T. Jiao, M. X. Shi, J. X. Liu, Y. B. Wang, W. F. Dong, C. Ding, T. X. Qin, H. Y. Liu, L. L. Wang, Z. Y. Zhang, P. Gao, Q. K. Xue, and Q. H. Xiong, Direct evidence of interfacial coherent electron-phonon coupling in single-unit-cell FeSe film on Nb-doped $SrTiO_3$, *Phys. Rev. Lett.* 135(12), 126903 (2025)
36. E. K. Ko, Y. J. Yu, Y. D. Liu, L. Bhatt, J. R. Li, V. Thampy, C. T. Kuo, B. Y. Wang, Y. Lee, K. Lee, J. S. Lee, B. H. Goodge, D. A. Muller, and H. Y. Hwang, Signatures of ambient pressure superconductivity in thin film $La_3Ni_2O_7$, *Nature* 638(8052), 935 (2025)
37. G. D. Zhou, W. Lv, H. Wang, Z. H. Nie, Y. Q. Chen, Y. Y. Li, H. L. Huang, W. Q. Chen, Y. J. Sun, Q. K. Xue, and Z. Y. Chen, Ambient-pressure superconductivity onset above 40 K in $(La,Pr)_3Ni_2O_7$ films, *Nature* 640(8059), 641 (2025)
38. Y. D. Liu, E. K. Ko, Y. J. Tarn, L. Bhatt, J. R. Li, V. Thampy, B. H. Goodge, D. A. Muller, S. Raghu, Y. J. Yu, and H. Y. Hwang, Superconductivity and normal-state transport in compressively strained $La_2PrNi_2O_7$ thin films, *Nat. Mater.* 24(8), 1221 (2025)
39. P. Li, G. D. Zhou, W. Lv, Y. Y. Li, C. M. Yue, H. L. Huang, L. Z. Xu, J. C. Shen, Y. Miao, W. H. Song, Z. H. Nie, Y. Q. Chen, H. Wang, W. Q. Chen, Y. B. Huang, Z. H. Chen, T. Qian, J. H. Lin, J. F. He, Y. J. Sun, Z. Y. Chen, and Q. K. Xue, Angle-resolved photoemission spectroscopy of superconducting $(La,Pr)_3Ni_2O_7/SrLaAlO_4$ heterostructures, *Natl. Sci. Rev.* 12(10), nwaf205 (2025)
40. H. L. Shi, Z. H. Huo, G. L. Li, H. Ma, T. Cui, D. X. Yao, and D. F. Duan, The effect of carrier doping and thickness on the electronic structures of $La_3Ni_2O_7$ thin films, *Chin. Phys. Lett.* 42(8), 080708 (2025)
41. Z. X. Deng, H. Yan, B. J. Wu, Y. J. Li, J. C. Zhang, Z. W. Zhu, C. L. Song, X. C. Ma, and Q. K. Xue, Tensile strain effect on superconductivity and thermally activated vortex motion in $Sr_{1-x}Eu_xCuO_{2+y}$ thin films, *Quantum Front.* 4(1), 18 (2025)
42. C. Si, Z. Liu, W. H. Duan, and F. Liu, First-principles calculations on the effect of doping and biaxial tensile strain on electron–phonon coupling in graphene, *Phys. Rev. Lett.* 111(19), 196802 (2013)
43. W. F. Pereira Júnior, W. F. da Cunha, R. T. J. Giozza, de Sousa, and Ribeiro, Irida-graphene: A new 2D carbon allotrope, *FlatChem* 37, 100469 (2023)
44. P. Giannozzi, S. Baroni, N. Bonini, M. Calandra, R. Car, C. Cavazzoni, D. Ceresoli, G. L. Chiarotti, M. Cococcioni, I. Dabo, A. Dal Corso, S. de Gironcoli, S. Fabris, G. Fratesi, R. Gebauer, U. Gerstmann, C. Gougoussis, A. Kokalj, M. Lazzeri, L. Martin-Samos, N. Marzari, F. Mauri, R. Mazzarello, S. Paolini, A. Pasquarello, L. Paulatto, C. Sbraccia, S. Scandolo, G. Sclauzero, A. P. Seitsonen, A. Smogunov, P. Umari, and R. M. Wentzcovitch, QUANTUM ESPRESSO: A modular and open-source software project for quantum simulations of materials, *J. Phys.: Condens. Matter* 21(39), 395502 (2009)
45. J. P. Perdew, K. Burke, and M. Ernzerhof, Generalized gradient approximation made simple, *Phys. Rev. Lett.* 77(18), 3865 (1996)
46. D. R. Hamann, Optimized norm-conserving Vanderbilt pseudopotentials, *Phys. Rev. B* 88(8), 085117 (2013)
47. M. Methfessel and A. T. Paxton, High-precision sampling for Brillouin-zone integration in metals, *Phys. Rev. B* 40(6), 3616 (1989)
48. S. Baroni, S. de Gironcoli, A. Dal Corso, and P. Giannozzi, Phonons and related crystal properties from density-functional perturbation theory, *Rev. Mod. Phys.* 73(2), 515 (2001)
49. G. Pizzi, V. Vitale, R. Arita, S. Blugel, F. Freimuth, G. Géranton, M. Gibertini, D. Gresch, C. Johnson, T. Koretsune, J. Ibañez-Azpiroz, H. Lee, J. M. Lihm, D. Marchand, A. Marrazzo, Y. Mokrousov, J. I. Mustafa, Y. Nohara, Y. Nomura, L. Paulatto, S. Ponc'e, T. Ponweiser, J. Qiao, F. Thöle, S. S. Tsirkin, M. Wierzbowska, N. Marzari, D. Vanderbilt, I. Souza, A. A. Mostofi, and J. R. Yates, Wannier90 as a community code: New features and applications, *J. Phys.: Condens. Matter* 32(16), 165902 (2020)
50. H. Lee, S. Poncé, K. Bushick, S. Hajinazar, J. Lafuente-Bartolome, J. Leveillee, C. Lian, J. M. Lihm, F. Macheda, H. Mori, H. Paudyal, W. H. Sio, S. Tiwari, M. Zacharias, X. Zhang, N. Bonini, E. Kioupakis, E. R. Margine, and F. Giustino, Electron–phonon physics from first principles using the EPW code, *npj Comput. Mater.* 9(1), 156 (2023)
51. F. Liu, P. B. Ming, and J. Li, Ab initio calculation of ideal strength and phonon instability of graphene under tension, *Phys. Rev. B* 76(6), 064120 (2007)
52. E. S. Penev, A. Kutana, and B. I. Yakobson, Can two-dimensional boron superconduct? *Nano Lett.* 16(4), 2522 (2016)
53. M. Gao, Q. Z. Li, X. W. Yan, and J. Wang, Prediction of phonon-mediated superconductivity in borophene, *Phys. Rev. B* 95(2), 024505 (2017)
54. M. Gao, X. W. Yan, J. Wang, Z. Y. Lu, and T. Xiang, Electron-phonon coupling in a honeycomb borophene grown on Al(111) surface, *Phys. Rev. B* 100(2), 024503 (2019)
55. C. Kamal and M. Ezawa, Arsenene: Two-dimensional buckled and puckered honeycomb arsenic systems, *Phys. Rev. B* 91(8), 085423 (2015)
56. X. Kong, M. Gao, X. W. Yan, Z. Y. Lu, and T. Xiang, Superconductivity in electron-doped arsenene, *Chin. Phys. B* 27(4), 046301 (2018)
57. H. Şahin, S. Cahangirov, M. Topsakal, E. Bekaroglu, E. Akturk, R. T. Senger, and S. Ciraci, Monolayer honeycomb structures of group-IV elements and III-V binary compounds: First principles calculations, *Phys. Rev. B* 80(15), 155453 (2009)
58. J. Maultzsch, S. Reich, C. Thomsen, H. Requardt, and P. Ordejon, Phonon dispersion in graphite, *Phys. Rev. Lett.* 92(7), 075501 (2004)
59. N. Bonini, M. Lazzeri, N. Marzari, and F. Mauri, Phonon anharmonicities in graphite and graphene, *Phys. Rev. Lett.* 99(17), 176802 (2007)
60. P. B. Allen, Neutron spectroscopy of superconductors, *Phys. Rev. B* 6(7), 2577 (1972)
61. P. B. Allen and R. C. Dynes, Transition temperature of strong coupled superconductors reanalyzed, *Phys. Rev. B* 12(3), 905 (1975)

62. S. Grimme, Semiempirical GGA-type density functional constructed with a long-range dispersion correction, *J. Comput. Chem.* 27(15), 1787 (2006)
63. J. Heyd, G. E. Scuseria, and M. Ernzerhof, Erratum: Hybrid functionals based on a screened Coulomb potential, *J. Chem. Phys.* 124(21), 219906 (2006)
64. M. Cococcioni and S. de Gironcoli, Linear response approach to the calculation of the effective interaction parameters in the LDA+U method, *Phys. Rev. B* 71(3), 035105 (2005)
65. Y. Cao, V. Fatemi, A. Demir, S. Fang, S. L. Tomarken, J. Y. Luo, J. D. Sanchez-Yamagishi, K. Watanabe, T. Taniguchi, E. Kaxiras, R. C. Ashoori, and P. Jarillo-Herrero, Correlated insulator behaviour at half-filling in magic-angle graphene superlattices, *Nature* 556(7699), 80 (2018)
66. Z. Ma, S. Li, M. M. Xiao, Y. W. Zheng, M. Lu, H. Liu, J. H. Gao, and X. C. Xie, Moiré flat bands of twisted few-layer graphite, *Front. Phys. (Beijing)* 18(1), 13307 (2022)
67. L. Li, M. Wu, and X. Lu, Correlation, superconductivity and topology in graphene moiré superlattice, *Front. Phys. (Beijing)* 18(4), 43401 (2023)
68. L. H. Tong, C. C. Xu, and L. J. Yin, Recent progress in scanning tunneling microscopy/spectroscopy characterization for magicangle twisted multilayer graphene, *Front. Phys. (Beijing)* 21(6), 065301 (2026)
69. Q. Y. Gu, D. Y. Xing, and J. Sun, Superconducting single-layer T-graphene and novel synthesis routes, *Chin. Phys. Lett.* 36(9), 097401 (2019)
70. Y. T. Kang, C. Lu, F. Yang, and D. X. Yao, Single-orbital realization of high-temperature $s^{\pm}$ superconductivity in the square octagon lattice, *Phys. Rev. B* 99(18), 184506 (2019)
71. Y. Yao, J. Li, J. Ye, F. Yang, and D. X. Yao, Electric field induced superconductivity in bilayer octagraphene, *Chin. Phys. Lett.* 42(6), 067504 (2025)
72. J. C. Ye, J. Li, D. Y. Zhong, and D. X. Yao, Possible superconductivity in biphenylene, *Chin. Phys. Lett.* 40(7), 077401 (2023)
73. W. H. Wan, Y. F. Ge, F. Yang, and Y. G. Yao, Phonon-mediated superconductivity in silicene predicted by first-principles density functional calculations, *Europhys. Lett.* 104(3), 36001 (2013)
74. Y. F. Ge, W. H. Wan, F. Yang, and Y. G. Yao, The strain effect on superconductivity in phosphorene: A first-principles prediction, *New J. Phys.* 17(3), 035008 (2015)
75. L. P. Zhang, Z. Y. Xu, X. J. Li, X. Zhang, M. Y. Qin, R. Z. Zhang, J. Xu, W. X. Cheng, J. Yuan, H. B. Wang, A. V. Silhanek, B. Y. Zhu, J. Miao, and K. Jin, Cascade excitation of vortex motion and reentrant superconductivity in flexible Nb thin films, *Chin. Phys. B* 32(4), 047302 (2023)
76. Y. Guo, Y. F. Zhang, X. Y. Bao, T. Z. Han, Z. Tang, L. X. Zhang, W. G. Zhu, E. G. Wang, Q. Niu, Z. Q. Qiu, J. F. Jia, Z. X. Zhao, and Q. K. Xue, Superconductivity modulated by quantum size effects, *Science* 306(5703), 1915 (2004)
77. T. Nishio, T. An, A. Nomura, K. Miyachi, T. Eguchi, H. Sakata, S. Lin, N. Hayashi, N. Nakai, M. Machida, and Y. Hasegawa, Superconducting Pb island nanostructures studied by scanning tunneling microscopy and spectroscopy, *Phys. Rev. Lett.* 101(16), 167001 (2008)
78. H. M. Zhang, Y. Sun, W. Li, J. P. Peng, C. L. Song, Y. Xing, Q. H. Zhang, J. Q. Guan, Z. Li, Y. F. Zhao, S. H. Ji, L. L. Wang, K. He, X. Chen, L. Gu, L. S. Ling, M. L. Tian, L. Li, X. C. Xie, J. P. Liu, H. Yang, Q. K. Xue, J. Wang, and X. Ma, Detection of a superconducting phase in a two-atom layer of hexagonal ga film grown on semiconducting GaN(0001), *Phys. Rev. Lett.* 114(10), 107003 (2015)
79. C. X. Zhao and J. F. Jia, Stanene: A good platform for topological insulator and topological superconductor, *Front. Phys. (Beijing)* 15(5), 53201 (2020)
80. J. Bekaert, A. Aperis, B. Partoens, P. M. Oppeneer, and M. V. Milošević, Evolution of multigap superconductivity in the atomically thin limit: Strain-enhanced three-gap superconductivity in monolayer MgB_2, *Phys. Rev. B* 96(9), 094510 (2017)
81. J. Bekaert, M. Petrov, A. Aperis, P. M. Oppeneer, and M. V. Milosevic, Hydrogen-induced high-temperature superconductivity in two-dimensional materials: The example of hydrogenated monolayer MgB_2, *Phys. Rev. Lett.* 123(7), 077001 (2019)
82. M. Gao, X. W. Yan, Z. Y. Lu, and T. Xiang, Strong-coupling superconductivity in LiB_2C_2 trilayer films, *Phys. Rev. B* 101(9), 094501 (2020)
83. L. Liu, X. Liu, P. Song, L. Zhang, X. Huang, W. Zhang, Z. Zhang, and Y. Jia, Surface superconductivity with high transition temperatures in layered $Ca_nB_{n+1}C_{n+1}$ films, *Nano Lett.* 23(5), 1924 (2023)
84. Y. M. Zhang, J. Y. Chen, J. Hao, M. L. Xu, and Y. W. Li, Conventional high-temperature superconductivity in σ-band driven metallized two-dimensional metal borocarbides, *Phys. Rev. B* 110(6), 064513 (2024)
85. W. X. Chen, Z. T. Liu, Z. H. Huo, G. Y. Dong, J. L. Cai, and D. F. Duan, High-temperature phonon-mediated superconductivity with T_c above 100 K in monolayer $Na(BC)_2$ and $K(BC)_2$, *Chin. Phys. Lett.* 41(11), 117403 (2024)
86. X. T. Jin, X. W. Yan, and M. Gao, First-principles calculations of monolayer hexagonal boron nitride: Possibility of superconductivity, *Phys. Rev. B* 101(13), 134518 (2020)
87. H. D. Liu, B. T. Wang, Z. G. Fu, H. Y. Lu, and P. Zhang, Three gap superconductivity with T_c above 80 K in hydrogenated 2D monolayer LiBC, *Phys. Rev. Res.* 6(3), 033241 (2024)
88. R. Q. Ku, L. Yan, J. G. Si, S. Y. Zhu, B. T. Wang, Y. D. Wei, K. J. Pang, W. Q. Li, and L. J. Zhou, Ab initio investigation of charge density wave and superconductivity in two-dimensional Janus 2H/1T-MoSH monolayers, *Phys. Rev. B* 107(6), 064508 (2023)
89. K. S. Novoselov, A. K. Geim, S. V. Morozov, D. Jiang, Y. Zhang, S. V. Dubonos, I. V. Grigorieva, and A. A. Firsov, Electric field effect in atomically thin carbon films, *Science* 306(5696), 666 (2004)
90. J. A. Marsden and M. M. Haley, Carbon networks based on dehydrobenzoannulenes. 5. Extension of two-dimensional conjugation in graphdiyne nanoarchitectures, *J. Org. Chem.* 70(25), 10213 (2005)

91. G. X. Li, Y. L. Li, H. B. Liu, Y. B. Guo, Y. J. Li, and D. B. Zhu, Architecture of graphdiyne nanoscale films, *Chem. Commun. (Camb.)* 46(19), 3256 (2010)
92. Q. D. Li, Y. Li, Y. Chen, L. L. Wu, C. F. Yang, and X. L. Cui, Synthesis of γ-graphyne by mechanochemistry and its electronic structure, *Carbon* 136, 248 (2018)
93. V. G. Desyatkin, W. B. Martin, A. E. Aliev, N. E. Chapman, A. F. Fonseca, D. S. Galvão, E. R. Miller, K. H. Stone, Z. Wang, D. Zakhidov, F. T. Limpoco, S. R. Almahdali, S. M. Parker, R. H. Baughman, and V. O. Rodionov, Scalable synthesis and characterization of multilayer γ-graphyne, new carbon crystals with a small direct band gap, *J. Am. Chem. Soc.* 144(39), 17999 (2022)
94. Q. T. Fan, L. H. Yan, M. W. Tripp, O. Krejčí, S. Dimosthenous, S. R. Kachel, M. Chen, A. S. Foster, U. Koert, P. Liljeroth, and J. M. Gottfried, Biphenylene network: A nonbenzenoid carbon allotrope, *Science* 372(6544), 852 (2021)
95. N. G. C. Astrath, F. Sato, F. Pedrochi, A. N. Medina, A. C. Bento, M. L. Baesso, C. Persson, and A. Ferreira da Silva, Band gap energy determination by photoacoustic spectroscopy under continuous light excitation, *Appl. Phys. Lett.* 89(23), 231926 (2006)
96. I. G. Lezama, A. Arora, A. Ubaldini, C. Barreteau, E. Giannini, M. Potemski, and A. F. Morpurgo, Indirect-to-direct band gap crossover in few-layer $MoTe_2$, *Nano Lett.* 15(4), 2336 (2015)
97. S. J. Zelewski and R. Kudrawiec, Photoacoustic and modulated reflectance studies of indirect and direct band gap in van der Waals crystals, *Sci. Rep.* 7(1), 15365 (2017)